Materials Today Bio 29 (2024) 101249

Contents lists available at ScienceDirect

Materials Today Bio

journal homepage: www.journals.elsevier.com/materials-today-bio

Three-dimensional gas-foamed scaffolds decorated with metal phenolic networks for cartilage regeneration

Yujie Chen [a,b,c,1], Wei Xu [d,1], Zhen Pan [a,b,c,1], Bohui Li [e,f], Xiumei Mo [g], Yucai Li [a,b,c], Jielin Wang [a,b,c], Yuan Wang [c], Zhenyuan Wei [a,b,c], Yicheng Chen [a,b,c], Zhaopu Han [a,b,c], Chen Lin [h], Yu Liu [e,f,***], Xiaojian Ye [a,b,c,*], Jiangming Yu [a,b,c,**]

[a] Laboratory of Key Technology and Materials in Minimally Invasive Spine Surgery, Tongren Hospital, Shanghai Jiao Tong University School of Medicine, Shanghai, 200336, China
[b] Center for Spinal Minimally Invasive Research, Shanghai Jiao Tong University, Shanghai, 200336, China
[c] Department of Orthopaedics, Tongren Hospital, Shanghai Jiao Tong University School of Medicine, Shanghai, 200336, China
[d] Department of Plastic Surgery, Qilu Hospital (Qingdao), Cheeloo College of Medicine, Shandong University, Qingdao, Shandong, 266035, China
[e] Plastic Surgery Institute, Shandong Second Medical University, Weifang, Shandong, 261053, China
[f] Shanghai Key Laboratory of Tissue Engineering, Department of Plastic and Reconstructive Surgery, Shanghai 9th People's Hospital, Shanghai Stem Cell Institute, Shanghai Jiao Tong University School of Medicine, Huangpu, Shanghai, 200001, China
[g] Shanghai Engineering Research Center of Nano-Biomaterials and Regenerative Medicine, State Key Laboratory for Modification of Chemical Fibers and Polymer Materials, College of Biological Science and Medical Engineering, Donghua University, Songjiang, Shanghai, 201600, China
[h] Department of General Surgery, Shanghai East Hospital, Tongji University School of Medicine, Pudong New Area, Shanghai, 200120, China

ARTICLE INFO

Keywords:
Cartilage repair
Inflammation
Metal phenolic networks
Electrospinning
Gas foaming
Nanofibers

ABSTRACT

Inflammation is a major impediment to the healing of cartilage injuries, yet bioactive scaffolds suitable for cartilage repair in inflammatory environments are extremely rare. Herein, we utilized electrospinning to fabricate a two-dimensional nanofiber scaffold (2DS), which was then subjected to gas foaming to obtain a three-dimensional scaffold (3DS). 3DS was modified with metal phenolic networks (MPNs) composed of epigallocatechin gallate (EGCG) and strontium ions (Sr^{2+}) to afford a MPNs-modified 3D scaffold (3DS-E). Gas-foamed scaffold exhibited multilayered structure conducive to cellular infiltration and proliferation. Compared to other groups, 3DS-E better preserved chondrocytes under interleukin (IL)-1β induced inflammatory environment, showing less apoptosis of chondrocytes and higher expression of cartilage matrix. Additionally, 3DS-E facilitated the regeneration of more mature cartilage *in vivo*, reduced cell apoptosis, and decreased the expression of pro-inflammatory cytokines.

Taken together, 3DS-E may offer an ideal candidate for cartilage regeneration.

1. Introduction

Articular cartilage damage induced by osteoarthritis, trauma, or various reasons significantly impair patient quality of life and can lead to disability if not promptly intervened [1]. Cartilage lacks vascular and neural tissue, rendering it with limited self-healing capabilities [2]. Clinically, techniques such as microfracture, autologous chondrocyte implantation (ACI), and matrix-assisted chondrocyte implantation (MACI) have been employed for cartilage repair [3]. However, these techniques need for multiple surgeries and face limitations such as donor site shortage or morbidity, and the formation of fibrocartilage, prompting the development of tissue engineering [4].

Scaffolds play a fundamental part in cartilage tissue engineering (CTE). Electrospinning, due to its versatility and high production

* Corresponding author. Laboratory of Key Technology and Materials in Minimally Invasive Spine Surgery, Tongren Hospital, Shanghai Jiao Tong University School of Medicine, Shanghai, 200336, China.
** Corresponding author. Center for Spinal Minimally Invasive Research, Shanghai Jiao Tong University, Shanghai, 200336, China.
*** Corresponding author. Plastic Surgery Institute, Shandong Second Medical University, Weifang, Shandong, 261053, China.
E-mail addresses: yuliu1211@163.com (Y. Liu), 732004380@shsmu.edu.cn (X. Ye), yjm_st@163.com (J. Yu).
[1] These authors contributed equally to this work.

https://doi.org/10.1016/j.mtbio.2024.101249
Received 20 May 2024; Received in revised form 3 September 2024; Accepted 13 September 2024
Available online 14 September 2024

efficiency, has been widely used in the construction of scaffolds for CTE [5,6]. However, conventional electrospun membranes, composed of densely packed fibers, hinder cell infiltration. A series of post-electrospinning treatments were developed for the fabrication of porous nanofibrous scaffolds, aiming to enhance scaffold porosity and create a looser nanofibrous structure [7]. Among these, gas foaming has recently gained prominence in the biomaterials field, with its main advantage being the efficient fabrication of 3D scaffolds with continuous, integrated multilayer structures. Gas foaming utilizes chemical reactions of gases to generate bubbles in situ, requiring simple equipment that is nearly universally applicable in all experimental settings [8,9]. Our previous research has demonstrated the capacity of gas-foamed scaffolds to support cell and tissue ingrowth, with modified gas-foamed scaffolds also showing significant advancements in maintaining chondrocyte phenotype and alleviating inflammation [10,11]. However, the bioactivity of gas-foamed scaffolds remains relatively simplistic, and their capacity for cartilage regeneration in inflammatory environments and the mechanisms of cartilage repair have not been intensively studied. Hence, the present study intends to construct gas foamed scaffolds with dual functionalities of alleviating inflammation and promoting cartilage matrix remodeling for cartilage tissue regeneration and to explore their potential repair mechanisms.

Inflammation causes an increase in cartilage matrix metalloproteinase content and a decrease in proteoglycan content, leading to tissue degradation [12]. Research indicates that incorporating functionalized peptides and growth factors into scaffolds can influence the phenotype and matrix expression of chondrocytes [13]. However, these bioactive factors and peptides present challenges such as high costs, short half-life, susceptibility to deactivation under physiological conditions, and concerns regarding their safety and stability. Compared to growth factors and peptides, inorganic ions possess advantages such as low cost and good stability. Studies have found that strontium ions (Sr^{2+}) can stimulate the production of proteoglycans through direct ionic effects independent of organic moiety [14]. Sr^{2+} could also enhance cellular activity by stimulating the expression of basic fibroblast growth factor [15]. EGCG is a polyphenolic compound extracted from plants, exhibiting biological properties such as antioxidation and reactive oxygen species (ROS) scavenging [16]. Composite scaffolds containing EGCG can reduce chondrocyte apoptosis, joint swelling, and synovial hyperplasia [17]. Additionally, EGCG can participate in scaffold surface modification through hydrogen bonding, with its hydroxyl groups providing chelation sites for further reaction with metal ions to form metal-phenolic networks (MPNs) [18]. Based on these studies, we hypothesize that constructing MPNs composed of strontium and EGCG on gas foamed scaffolds can enhance the scaffolds' bioactivity, achieving a synergistic effect of attenuating inflammation and enhancing cartilage ECM synthesis for cartilage regeneration.

Hence, this study aims to construct MPNs-modified 3D gas foamed nanofiber scaffolds and assess their capabilities in cartilage protection and regeneration. Herein, we fabricated a 3D scaffold by electrospinning combined with gas foaming treatment, and 3D scaffold was further modified with MPNs composed of EGCG/Sr^{2+}. The morphology, physicochemical properties, antioxidant capacity, and drug/ion release behaviors of scaffolds were extensively studied. Additionally, the scaffolds' capacities for anti-apoptosis, inflammation alleviation, and ECM secretion were investigated.

2. Materials and methods

2.1. Materials

Poly(L-lactide-co-ε-caprolactone) (PLCL, M_w = 300 kDa, L-lactide acid to ε-caprolactone mole ratio of 50:50) was purchased by Jinan Daigang Biomaterial Co., Ltd., Jinan, China. Epigallocatechin gallate (EGCG) was supplied by Bide Pharmatech Ltd., Shanghai, China. Hexafluoroisopropanol (HFIP) was obtained from Shanghai Darui Fine Chemical Co., Ltd., Shanghai, China. Cocoon of *B. mori silkworm* was purchased from Huzhou Silk Co., Ltd., Huzhou, China. Strontium chloride hexahydrate ($SrCl_2 \bullet 6H_2O$) was purchased from Macklin Biochemical Co., Ltd., Shanghai, China.

2.2. Fabrication of nanofiber scaffolds

PLCL and SF were dissolved in HFIP in a mass ratio of 8:2 to form a homogenous solution with a total weight of 10 % (w/v). The parameters were set to rate of 1.2 mL/h, voltage of 12 kV, and receiving distance of 15 cm. The environmental temperature was maintained between 20 °C and 30 °C, and the relative humidity was kept at 30 %–40 %. PLCL/SF membranes (2DS) were collected on aluminium foil by electrospinning [19]. To avoid deformation on the edges, 2DS mats were first cut into rectangle shape (1 cm × 1 cm × 1 mm) in the liquid nitrogen. Then, these rectangular 2DS were immersed in 0.5 M $NaBH_4$ aqueous solution at room temperature for 30 min. Expanded scaffolds were then rinsed and freeze-dried to finally obtain 3D PLCL/SF scaffolds (3DS). To obtain MPNs modified 3D scaffolds (3DS-E), 3DS with rectangle shape were immersed in the EGCG (concentration, 1 mg/mL) with 0.1 M $SrCl_2 \bullet 6H_2O$ for 10 min and then freeze-dried after water rinsing according to previous studies [20,21].

2.3. Characterization

The density and porosity of scaffolds were measured according to previously reported methods [10,22]. The morphology, elemental and functional group of the scaffolds were analyzed using SEM, EDS/XPS and FTIR, respectively. For the specific brands and origins of the machines, please see Table S1. 2,2-diphenyl-1-picrylhydrazyl (DPPH) assay was used to assess the antioxidant activity of scaffolds.

The mechanical properties of different specimens were recorded with a universal materials test machine (HY-940FS, Hengyu Instrument, Shanghai, China). 2DS, 3DS and 3DS-E underwent tension until rupture at 5 mm/min. Compression testing, applied to square-shaped 3DS and 3DS-E samples (side length: 10 mm; thickness: 3 mm), reached a compressive strain of 50 % at 1 mm/min. The kinetics of EGCG release in 3DS-E was monitored over 16 weeks period. The concentration of EGCG was analyzed by UV/vis spectrophotometer (JASCO V530, JASCO, Japan), and the concentration of Sr^{2+} from was analyzed by inductively coupled plasma-atomic emission spectrometry (ICP-AES, Leeman, USA).

2.4. In vitro evaluation of scaffold biocompatibility

Sterilized 2DS, 3DS and 3DS-E were placed in a 24-well plate. Chondrocyte suspension was evenly dropped to each scaffold (3.0×10^4 cells/well) to conduct live/dead, cell seeding efficiency, proliferation and cell infiltration assays. The cell seeding efficiency was evaluated using a previously described method [23]. After the cells incubation on scaffolds for 4 h, the unattached cells were counted and calculate cell seeding efficiency (S) according to Eq. (1):

$$S\ (\%) = (S1\ -\ S2)\ /\ S1 \times 100\% \quad (1)$$

where S1 is the total number of cells and S2 is the number of lost cells.

Cell proliferation assay was detected by cell counting kit 8 (CCK-8) assay. Cell infiltration was evaluated by fixing cell-laden scaffolds with 4 % paraformaldehyde (PFA) and performing with hematoxylin and eosin (H&E) staining. IL-1β (10 ng/mL) was used to stimulate inflammation and chondrocytes were cultured with scaffold extracts. 3DS or 3DS-E (1 mg/mL) were immersed in culture medium for 7 days, and the supernatants were used to culture IL-1β treated chondrocytes. In blank group, chondrocytes were cultured with medium without scaffold extracts. A control group included chondrocytes cultured without either scaffold extracts or IL-1β.

Cell viability were evaluated through a live/dead assay and TUNEL

staining was performed to elucidate apoptosis. Chondro-protective capacities of different groups in an inflammatory environment were determined using real-time quantitative polymerase chain reaction (qPCR). After treating with 10 ng/mL IL-1β, chondrocytes were incubated for 24 h with 3DS or 3DS-E extracts. Then, isolate the total mRNA using TRIzol reagent, and 500 ng of RNA was used to synthesize cDNA using PrimeScript RT reagent kit (TaKaRa, Japan). The cDNA was mixed with SYBR Premix Ex Taq (TaKaRa, Japan), and transcript levels were evaluated by qPCR performed with Applied Biosystems QuantStudio™ 5 Real-Time PCR System (Applied Biosystems, Waltham, MA, USA) following the manufacturer protocols. All primer sequences were listed in Table S2. The mRNA expression levels of Bcl-2 associated X protein (Bax), Caspase-9, B-cell lymphoma-2 (Bcl-2), collagen II (COL II), aggrecan (ACAN), tumor necrosis factor-alpha (TNF-α), interleukin-1 beta (IL-1β), matrix metalloproteinases 13 (MMP13), Adamalysin-like metalloproteinases with thrombospondin (TS) motifs (ADAMTS)-5, nuclear factor E2-related factor 2 (Nrf2), superoxide dismutase (SOD) and heme oxygenase-1 (HO-1) and β-actin were determined. The expression levels of genes were relative to β-actin and calculated by $-2^{\Delta\Delta Ct}$ method.

To evaluate inflammatory response, chondrocytes were fixed, permeabilized, and blocked before incubation with primary antibodies against MMP13 or COL II. After secondary antibody incubation and DAPI staining, the images were observed with a fluorescence microscope.

2.5. Articular cartilage regeneration in vivo

Animal experiments were conducted with the approval of the Ethics Committee of Shanghai Tongren Hospital (A2023-050-01). First, divide rabbits (4-month-old, 3 kg male New Zealand white rabbits) into three groups (n = 4). Rabbits were anesthetized using a 3 % pentobarbital solution (30 mg/kg). Subsequently, a full-thickness cartilage defect (diameter = 4 mm and depth = 3 mm) was created at the center of the trochlear groove. Implant 2DS, 3DS and 3DS-E into the defects and suture the incisions. After surgery, keep the animals in separate cages and euthanize at 12 weeks to harvest the femur condyle.

To assess the regeneration capability, the collected samples were imaged and evaluated using the International Cartilage Repair Society (ICRS) macroscopic scoring criteria. Collected specimens were fixed, decalcified and then embedded. The sections were subjected to immunohistochemical staining (COL I and COL II) and histological staining (H&E, Safranin-O/fast green (Saf-O/FG)) [11]. The histology of defect sections was further evaluated using Modified O'Driscoll histological scoring and Mankin score by three independent observers, with criteria detailed in the supplementary information (Table S3–S5).

Chondrocyte apoptosis within the knee joint cartilage was determined using the TUNEL assay. Sections were fixed with 4 % PFA, washed with PBS, incubated with 0.1 % sodium citrate buffer, then with terminal deoxynucleotidyl transferase (TDT) at 37 °C in darkness. Subsequently, anti-digoxigenin conjugate (fluorescein) staining was performed and nuclei were counterstained with DAPI. The apoptotic chondrocytes percentage was quantified as the ratio of fluorescein-positive to total nuclei. Immunofluorescence staining was performed to investigate inflammation. Sections were blocked and incubated with respective primary antibodies overnight, followed by incubation with fluorescent-labeled secondary antibodies and observed under a fluorescence microscope. Synovial fluid was collected, centrifuged, and the supernatants were stored at −80 °C. IL-1β levels were quantified using a rabbit IL-1β enzyme-linked immunosorbent assay (ELISA) Kit (R&D Systems, USA) in accordance with manufacturer's instructions.

2.6. Statistical analysis

The data were expressed as mean ± standard deviation (SD) and analyzed using one-way analysis of variance (ANOVA) followed by Tukey's post-hoc test or Student's t-test where appropriate. The statistical significance of all data was considered at p values < 0.05.

3. Results

3.1. Scaffold fabrication and characterization

The fabrication process of the gas-foamed scaffolds was depicted in Fig. 1. We synthesized 3D nanofibrous scaffolds via an approach that integrated electrospinning with gas foaming technology. Subsequently, these 3D scaffolds were submerged in a solution containing EGCG and Sr^{2+}. EGCG can interact with proteins via its pyrogallol hydroxyl groups. Moreover, the adjacent hydroxyl groups in EGCG provide chelation sites, enabling reactions with diverse metal ions, leading to the formation of MPNs.

Fig. 2A showed the gross appearance and SEM photographs of 2DS, 3DS and 3DS-E. After gas foaming, 3DS and 3DS-E with an approximate thickness of 3 mm were yielded. Each scaffold displayed a distinct nanofibrous architecture, while 2DS showed densely packed fibers on both the surface and cross-section. By contrast, 3DS and 3DS-E exhibited an interconnected, layered structure with a loose nanofiber topography and more pronounced pores on their surface. Notably, modification of MPNs on 3DS-E led to the presence of clustered particles on both the surface and cross-section.

Fig. 2B–D showed the physical properties including fiber diameter, gap distance, and pore size across scaffold type. The gas foaming had a negligible impact on the fiber diameter (2DS, 405 ± 110 nm; 3DS, 461 ± 138; 497 ± 100 nm), yet it resulted in larger gaps and pore sizes in the 3D scaffolds in comparison with the pristine membranes. Specifically, the inter-fiber gaps widened from a pre-foaming average of 5.63 ± 1.61 μm in 2DS to 49.81 ± 20.65 μm in 3DS and 46.62 ± 20.07 μm in 3DS-E, as shown in Fig. 2E. After expansion, pore sizes also expanded in 3DS (47.37 ± 14.61 μm^2) and 3DS-E (45.47 ± 16.33 μm^2), surpassing those of 2DS (18.19 ± 5.53 μm^2) as demonstrated in Fig. 2F. Changes in scaffold density and porosity pre- and post-foaming were detailed in Fig. 2G and H. The density of scaffolds decreased markedly from 0.175 g/cm^3 in 2DS to 0.033 and 0.034 g/cm^3 in 3DS and 3DS-E respectively, while porosity rose from 51.41 % in 2DS to 77.37 % and 76.87 % of 3DS and 3DS-E.

The elements of C, O, Sr on the 3DS-E surface were detected by SEM equipped with EDS. The EDS mapping predominantly localized strontium (visualized in blue) within the newly formed particles (Fig. 3A). FTIR further detailed the chemical makeup of different scaffolds (Fig. 3B). The EGCG demonstrated a broad absorption band at 3345 cm^{-1}, which were ascribed to the vibration of the O–H linkage of phenolic and hydroxyl groups. Additional EGCG signature peaks were noted at 825, 1148, 1225, 1521, 1620 and 1692 cm^{-1}, corresponding to vibrational patterns of C–H alkenes, C–OH alcohols, –OH aromatic, C=C aromatic ring, C=C alkenes and carbonyl stretching of the gallic acid [24]. Both 2DS and 3DS presented similar spectral patterns, showing characteristic peaks of PLCL and SF. The peaks at 1639 cm^{-1} and 1520 cm^{-1} were attributed to amide I and amide II bonds in SF. Absorption bands at 2938 and 1756 cm^{-1} were ascribed to the $–CH_2–$ stretching vibration and the ester carbonyl vibrations of PLCL. 3DS-E also exhibited a broad band appeared at 3345 and 825 cm^{-1}, which were assigned to the O–H and C–H alkenes vibrations from the EGCG. Notably, the amide I bond shifted from 1639 cm^{-1} to 1622 cm^{-1}, consistent with previous findings that EGCG presence attenuated amide I absorption [25]. The FTIR data confirmed that the gas foaming process did not induce chemical reactions among components and the EGCG was successfully modified on scaffolds.

In the XPS analysis, 3DS-E exhibited Sr 3d spectrum while 2DS and 3DS were devoid of it, indicative of an interaction between the nanofiber and the EGCG/Sr^{2+} MPNs (Fig. 3C). Mechanical properties were assessed through compression and tension tests. Fig. 3D revealed the resilience of 3DS-E, which recovered its original form after varied compression levels. Compressive stress–strain curves at 50 %

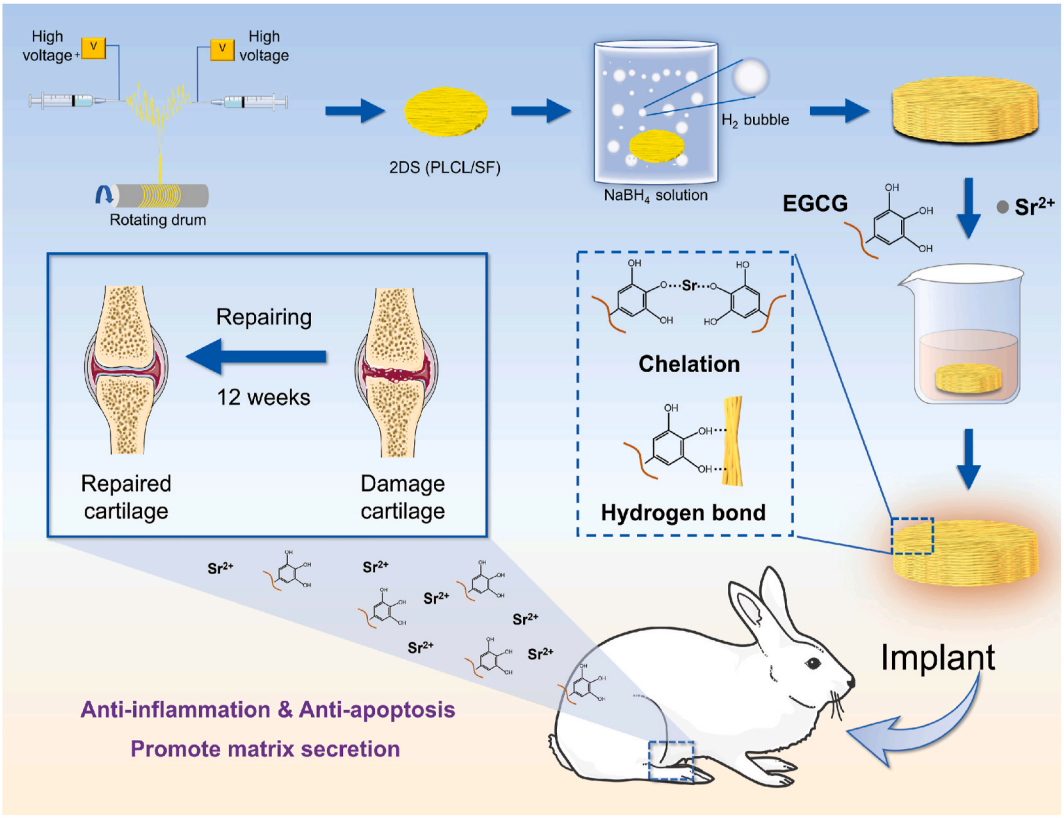

Fig. 1. Schematic diagram of the fabrication process of 3DS-E.

deformation for 3DS and 3DS-E were presented in Fig. 3E, with the corresponding compressive moduli determined to be 3.69 ± 0.51 kPa and 3.95 ± 0.55 kPa for 3DS and 3DS-E (Fig. 3F). The tensile properties were showed in Fig. 3G, with 2DS manifesting superior mechanical performance compared to the 3D scaffolds, as depicted through elastic modulus (E), ultimate tensile strength (UTS), and elongation at break (Eb) in Fig. 3H–J. Nevertheless, 3DS and 3DS-E revealed comparable tensile properties (for 3DS, E = 110.66 ± 12.33 kPa, UTS = 60.42 ± 3.39 kPa, and Eb = 37.62 ± 4.48 %; for 3DS-E, E = 111.47 ± 18.74 kPa, UTS = 59.22 ± 8.69 kPa, and Eb = 34.74 ± 3.09 %).

Fig. 3K demonstrated the release kinetics of EGCG from 3DS-E, with an initial 33.61 % release on day one and reached 72.31 % within 9 days, followed by a sustained release leading to an 77.71 % total release by day 28. The release pattern for Sr^{2+} was exhibited in Fig. 3L, showing a rapid initial release (36.78 % on the first day, reaching 80.46 % after 9 days) and leading to 90.81 % release after 28 days of immersion. These findings suggested a sustained EGCG and Sr^{2+} release from 3DS-E.

The degradation trends of 2DS, 3DS and 3DS-E over a 16-week span were presented in Fig. S1. All groups displayed negligible weight differences over the initial 4 weeks. At week 8, weight losses of 7.1 ± 2.2 %, 12.6 ± 1.8 %, and 12.8 ± 2.1 % were noted for 2DS, 3DS, and 3DS-E, respectively, and 24.6 ± 2.6 %, 37.7 ± 3.2 %, and 36.9 ± 2.4 % at week 16, respectively. The faster degradation rates observed in the 3D scaffolds can likely be attributed to their multilayered porous designs, which facilitate more expansive nanofiber interactions with hydrolytic processes, thereby accelerating degradation.

3.2. *In vitro cytocompatibility studies*

The antioxidant property of different scaffolds was explored utilizing the DPPH radical scavenging assay. As shown in Fig. 4A, 2DS achieved a radical inhibition rate of a modest 3.33 % and 4.61 % after 24 and 48 h incubation, and 3DS reached comparable 3.41 % and 5.22 % after 24 h and 48 h incubation. Inherent antioxidant capacities of SF attributed to its tyrosine and tryptophan composition, contributed a minor 5.6 % antioxidant effect [26]. In contrast, 3DS-E exhibited a pronounced ability to scavenge free radicals, with rates of 53.74 % and 70.68 % after incubations of 24 and 48 h, respectively.

After 4 h of *in vitro* incubation, the cell seeding efficiency on 3D scaffolds far outstripped that of 2DS, as illustrated in Fig. 4B. CCK-8 assay revealed that chondrocytes proliferated more effectively on the 3D scaffolds than 2DS, while 3DS-E showed a slight downturn in cellular proliferation compared to 3DS (Fig. 4C). Live/dead staining demonstrated no obvious cytotoxicity in all the scaffolds (Fig. 4D and E). H&E staining showed more cellular infiltration in 3D scaffolds in contrast to 2DS, with quantitative metrics revealing a more profound infiltration depth for chondrocytes on 3D scaffolds—a depth of 83.79 ± 20.60 μm for 3DS and 88.91 ± 17.59 μm for 3DS-E, compared to a mere 19.27 ± 8.09 μm for 2DS, as depicted in Fig. 4F–H.

Our study utilized IL-1β to simulate an inflammatory microenvironment. Given the identical compositions of 2DS and 3DS, the extracts of 3DS and 3DS-E were used to explore the chondro-protective capacities of various groups. Live/dead cell assay demonstrated that IL-1β mediated the augmentation in the number of dead cells, whereas the number of dead cells in the 3DS-E group was less than that in the blank and 3DS groups (Fig. 5A and B). 3DS-E also alleviated IL-1β-induced chondrocyte apoptosis, evidenced by a lower TUNEL-positive nucleus percentage (17.25 %) relative to both the 3DS (45.12 %) and blank groups (47.96 %) (Fig. 5C and D). As shown in Fig. 5E–G, chondrocytes co-cultured with the leachate of 3DS-E exhibited higher levels of expression in anti-apoptotic genes Bcl-2 when compared with blank and 3DS groups. 3DS-E also down-regulated the expression of apoptotic genes Bax and Caspase-9 in chondrocytes than that of blank and 3DS groups, suggesting that 3DS-E may have a positive effect on inhibiting chondrocyte apoptosis in the inflammatory environment.

Immunofluorescence staining showed that MMP13 fluorescence

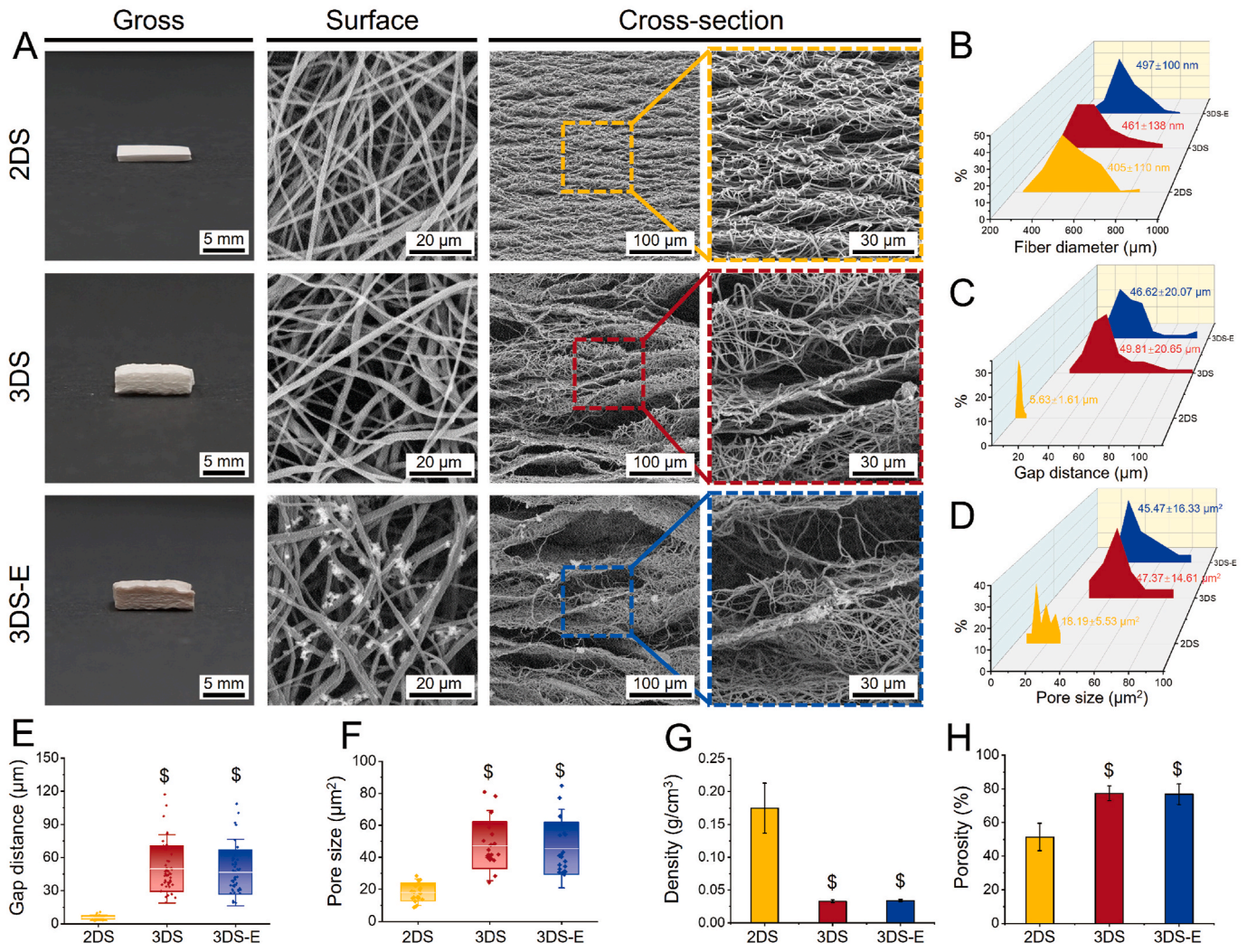

Fig. 2. Physical properties of 2DS, 3DS and 3DS-E. (A) Gross view and SEM images of 2DS, 3DS and 3DS-E. The distributions of fiber diameter (B), gap distance (C) and pore size (D) of 2DS, 3DS and 3DS-E (n = 50). Gap distance (E) and pore size (F) quantification of 2DS, 3DS and 3DS-E (n = 50). Density (G) and porosity (H) of 2DS, 3DS and 3DS-E (n = 3). ($, % indicate $p < 0.05$ versus 2DS and 3DS, respectively.)

signal was elevated in chondrocytes after IL-1β treatment, while COL II was decreased (Fig. 6A and B). 3DS-E significantly lessened MMP13 fluorescence, while increasing COL II signal intensity in contrast to 3DS (Fig. S2). Typically, ADAMTS5 and MMP13 are associated with cartilage matrix degradation, whereas a healthy chondrocyte signature includes abundant COL II and ACAN. 3DS-E markedly decreased the mRNA expression levels of MMP13, IL-1β, TNF-α and ADAMTS5, and reversed the decreased mRNA expression levels of COL II and ACAN in chondrocytes after IL-1β treatment (Fig. 6C–H). 3DS-E presented the upregulation of Nrf2, SOD-1, and HO-1 mRNA level than those of blank and 3DS groups, indicating the activation of Nrf2 pathway (Fig. 6I–L). In summary, 3DS-E modulated inflammation via the Nrf2 pathway and mitigating ECM degeneration.

3.3. *In vivo evaluation of articular cartilage repair*

After 12 weeks transplantation, non-treated group exhibited obvious cartilage defect and only little neo-tissue could be found in the defect area. In the 2DS groups, defects were filled with white neo-cartilage tissue with fine fissure. In the 3DS groups, newly-formed cartilage-like tissues were partially integrated with the adjacent tissue, while some small fissure remaining. By contrast, in 3DS-E group, the neo-cartilage tissue integrated with the bordering tissues with a smooth and flat surface (Fig. 7A).

Subsequent histological and immunohistochemical assessments of the harvested samples highlighted differing regenerative outcomes. In non-treated and 2DS groups, only sparse fibrous tissues occupied the defect zone, and neo-tissue was poorly integrated with native cartilage, with diminished Saf-O and COL II staining and an abundance of COL I. For 3DS, the new tissue formed was thin, lacking the deposition of mature cartilage ECM. The neocartilage tissue in the 3DS-E exhibited substantial ECM deposition and thorough integration with native cartilage, reflective of optimal cartilage regeneration.

The detail-rich magnified image demonstrated that the chondrocytes within the 3DS-E displayed a distinctive lacunar structure, complete with marked ECM accumulation and intensive COL II staining resembling natural cartilage (Fig. 7B). The ICRS macroscopic score of 3DS-E group (8.25 ± 0.5) was superior to other groups (2.0 ± 0.8 for non-treated group, 2.5 ± 0.6 for 2DS, and 5.2 ± 0.5 for 3DS) (Fig. 7C). Analogously, modified O'Driscoll histological scores were 6.8 ± 1.2, 7.5 ± 1.3, 12.5 ± 1.8 and 16.8 ± 1.3 for the non-treated, 2DS, 3DS and 3DS-E groups, indicating a markedly superior repair outcomes of 3DS-E than that of other groups (Fig. 7D). Mankin score further demonstrated the best therapeutic effect in 3DS-E group (4.0 ± 0.8) in contrast to non-treated group (9.8 ± 0.5), 2DS (8.5 ± 1.3) and 3DS (7.0 ± 1.2) (Fig. 7E). Quantitative analysis results showed that compared to non-treated, 2DS and 3DS groups, 3DS-E exhibited higher secretion of COL II and lower expression of COL I, indicating that the newly formed

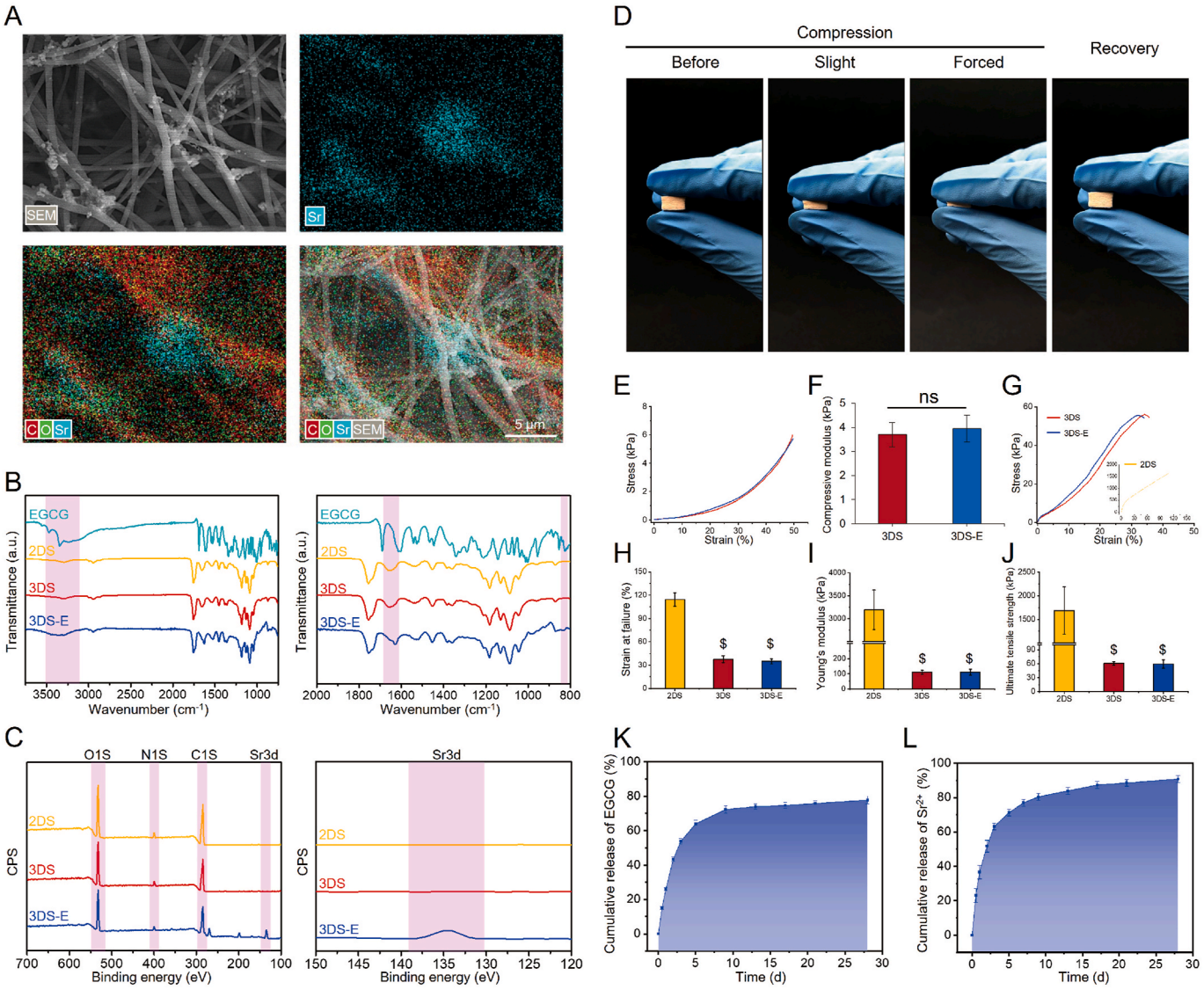

Fig. 3. Characterization of the composition, mechanical properties, and release behavior of the active components of the scaffold. (A) Representative elemental mapping of the 3DS-E. (B) ATR-FTIR spectra of EGCG, 2DS, 3DS and 3DS-E. (C) XPS spectra of 2DS, 3DS and 3DS-E. (D) Photographs showing the resilience of the 3DS-E. Representative curves (E) of the compression test with $\varepsilon = 50$ % and compressive modulus (F) of 3D scaffolds (n = 3). Representative tensile stress-strain curves (G), elongation at break (H), Young's modulus (I), and ultimate tensile strength (J) of 2DS, 3DS and 3DS-E (n = 3). Release of EGCG (K) and Sr^{2+} (L) from 3DS-E (n = 3). ($, % indicate $p < 0.05$ versus 2DS and 3DS, respectively.)

cartilage resembled natural cartilage rather than fibrocartilage (Fig. 7F–H).

TUNEL staining was performed to evaluate the apoptosis of articular chondrocytes. 3DS-E revealed diminished TUNEL-positive expression relative to the 2DS and 3DS groups (Fig. 8A). Quantitative analysis revealed that the number of TUNEL-positive cells was significantly reduced in the 3DS-E group (20 %) compared to the 2DS (47 %) and 3DS (35 %) groups (Fig. 8B). The inflammatory response in articular cartilage was evaluated by TNF-α and IL-1β immunofluorescence staining, where 3DS-E exhibited a weaker fluorescence expression than 2DS and 3DS (Fig. 8C–E). ELISA assay further confirmed the milder inflammatory response of 3DS-E (Fig. 8F). Conclusively, 3DS-E could attenuate intra-articular inflammation and chondrocyte apoptosis effectively.

4. Discussion

In this study, we have fabricated a 3D gas-foamed nanofiber scaffold modified with MPNs composed of strontium ions and EGCG. 3DS-E facilitates the release of polyphenols and ions, fulfilling the simultaneous requirements for inflammation mitigation and cartilage matrix remodeling. Moreover, the multilayered structure is favorable to cell proliferation and infiltration, aiding in maintaining the chondrocyte phenotype. Our research underscores the critical importance of concurrent inflammation relief and matrix remodeling, elucidating the therapeutic potential of 3D nanofiber scaffolds modified with bioactive ions and polyphenols for cartilage tissue regeneration.

Electrospinning is an efficient nanofiber manufacturing technique; however, normal electrospun membranes tend to have a thin thickness and a dense surface, which poses a limitation to cell infiltration. To increase scaffold porosity and achieve a porous 3D structure, direct enhancement methods like wet electrospinning, multilayer electrospinning, and sacrificial template methods have been developed [8]. Although these direct methods bypass post-processing steps, they offer only limited improvements in porosity. Post-processing methods, such as short fiber assembly, electrospinning combined with 3D printing, and electrospraying, can produce loose 3D scaffolds. These methods offer broad material applicability and allow for controllable scaffold shapes and sizes, but they require specialized equipment, such as homogenizer

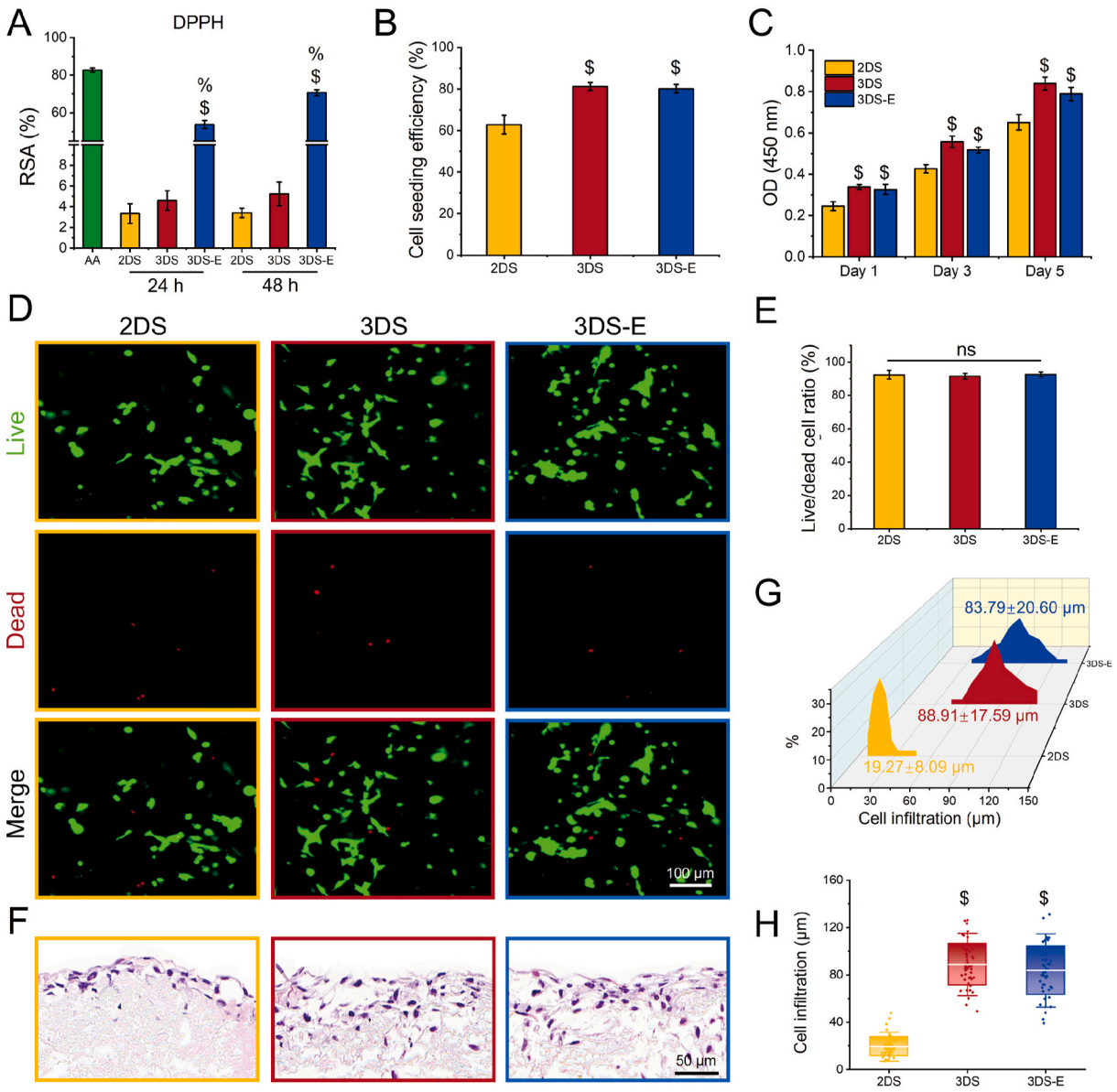

Fig. 4. Cytocompatibility of scaffolds *in vitro*. (A) Radical scavenging activity of 2DS, 3DS, 3DS-E (n = 3). Cell seeding efficiency (B), proliferation (C) and live/dead staining (D) of chondrocytes cultured on different scaffolds (n = 3). (E) Quantification of live cell/dead cell ratio (n = 3). (F) H&E staining reveals chondrocyte distribution in 2DS, 3DS, and 3DS-E. Distribution (G) and quantification (H) of cell infiltration depth on 2DS, 3DS, and 3DS-E. ($, % indicate $p < 0.05$ versus 2DS and 3DS.)

and 3D printers. Gas foaming, on the other hand, can yield integrated multilayer 3D scaffolds without disrupting the continuous fiber structure of the nanofiber membrane. The size can be tailored through time control or utilization of molds, and the multilayer nanofiber structure provides ample space for cell growth and infiltration, rendering it a simple yet immensely potential-rich technique for fabricating 3D porous scaffolds. The 3D scaffolds obtained using the gas foaming technique in this research exhibit a multilayer structure and good cell infiltration properties, offering pivotal support for matrix remodeling and tissue regeneration. We use a combination of PLCL/SF as the basic materials for the 3D scaffolds, which has proven successful in various tissue regeneration applications, such as tendon, skin, blood vessel, and nerve [27]. PLCL, a biodegradable biomaterial with mechanical elasticity, has been reported to promote cartilage repair through cellular mechanotransduction [28]. SF, a protein-based natural material, increases the hydrophilicity and biocompatibility of composite scaffolds, overcoming the expansion limitations of PLCL during gas foaming due to its hydrophobicity [29].

Biocompatibility and high porosity are fundamental factors for cell survival and ingrowth within scaffolds. Chondrocytes were able to stably survive on both 2D and 3D scaffolds, indicating that all scaffolds possessed negligible cytotoxicity. Chondrocytes proliferated faster on the 3D scaffolds, likely due to the larger porosity giving more binding sites for cellular growth. Notably, although not significant, cell numbers on 3DS-E were lower compared to 3DS, which may be attributed to catechins inhibiting key enzymes in the cell cycle, potentially temporarily suppressing cell metabolism [30]. However, under inflammatory conditions, 3DS-E displayed superior cell protective abilities. The coordination of metal ions with EGCG stabilized the MPNs within the scaffold, and when the ionic interactions were destroyed, EGCG was protonated and thus released [31]. By releasing EGCG, 3DS-E not only eliminated free radicals but also downregulated pro-apoptotic genes and upregulated anti-apoptotic gene expression. Studies have indicated that phenolic compounds may remove the free radicals plausibly through

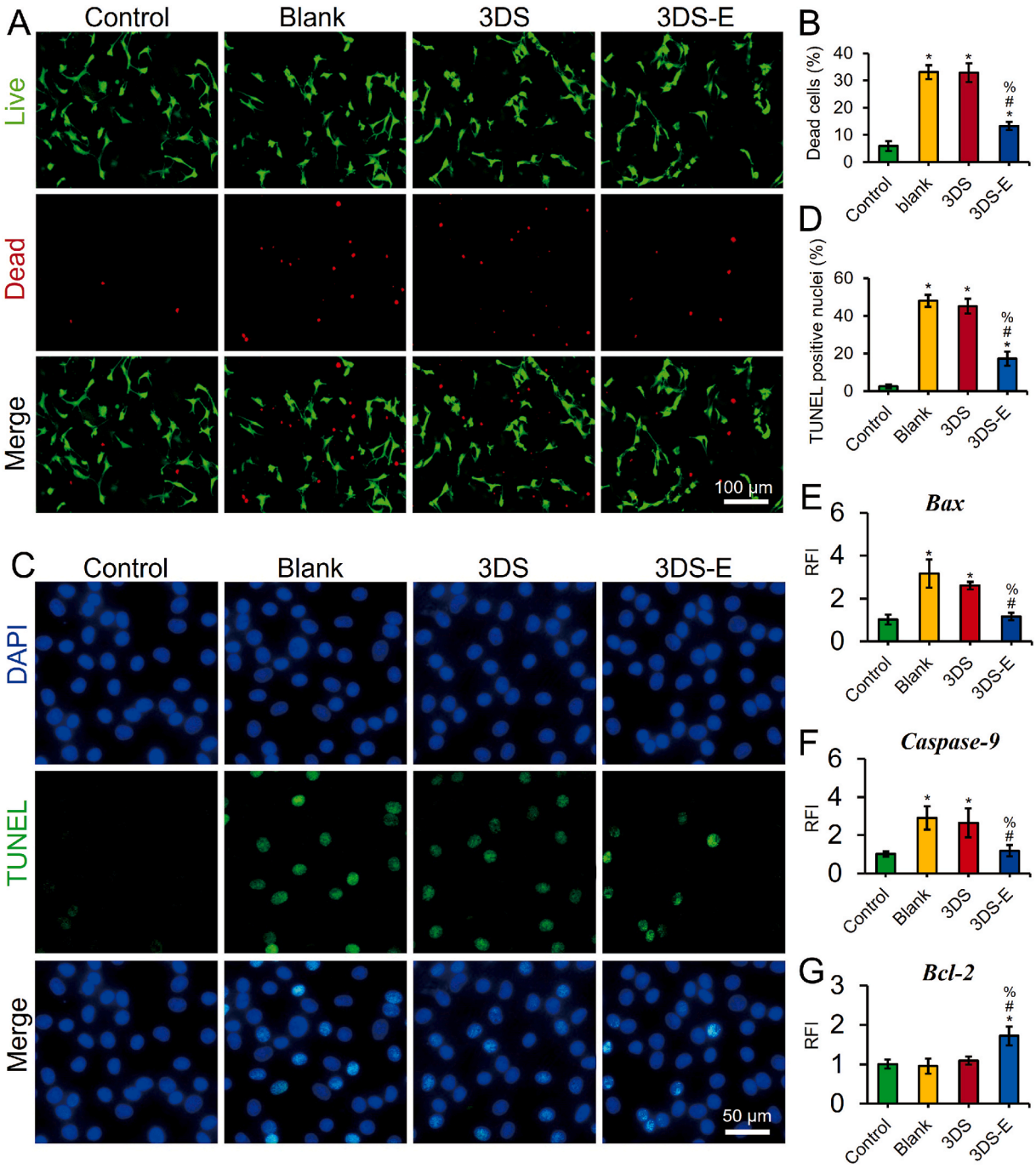

Fig. 5. Chondro-protective capacity of scaffolds. Live/dead staining (A) and percentage of the dead cells (B) (n = 3). TUNEL assay (C) and percentage of positive cells (D) (n = 3). Relative expression of genes Bax (E), Caspase-9 (F), and Bcl-2 (G) in chondrocytes (n = 3). (*, #, % indicate $p < 0.05$ versus control, blank, 3DS.)

phenol-mediated aromatic ring resonance stabilization, resulting in the stimulation of cellular anti-apoptotic/oxidant signaling pathways [32].

When cartilage defects occur, acute inflammation is triggered, initiating a healing cascade reaction. Without timely balancing inflammation and anti-inflammation, the persistent release of inflammatory cytokines in a chronic inflammatory environment will hinder the synthesis of cartilage matrix [33]. Therefore, designing a scaffold capable of alleviating inflammation and decreasing ECM degradation is crucial. Herein, IL-1β was used to stimulate the inflammatory response after joint damage. The presence of IL-1β accelerated the degradation of ECM, but 3DS-E significantly downregulated inflammatory genes expression in chondrocytes and promoted matrix secretion, indicating a positive effect of MPNs on the improvement of the microenvironment for cartilage regeneration. Nrf2 is a member of the capncollar-basic leucine zipper (CNC-bZIP) transcription activator family and exists in cytoplasm as inactivation under physiological conditions. In response to inflammation, the conformation of Nrf2 changes, translocating into the nucleus, where it binds to antioxidant response elements (ARE) and regulates the expression of antioxidative enzymes SOD-1 and HO-1 [34]. 3DS-E can protect chondrocytes in an inflammatory environment by activating the Nrf2 pathway, upregulating the expression of SOD-1 and HO-1, reducing cartilage matrix degradation, thus creating a favorable microenvironment for cartilage remodeling. Scaffold incorporating specific ions represents an emerging method for tissue repair [35]. Strontium, as an essential trace element, has been used in the management of cartilage diseases for decades [36]. In addition to promoting

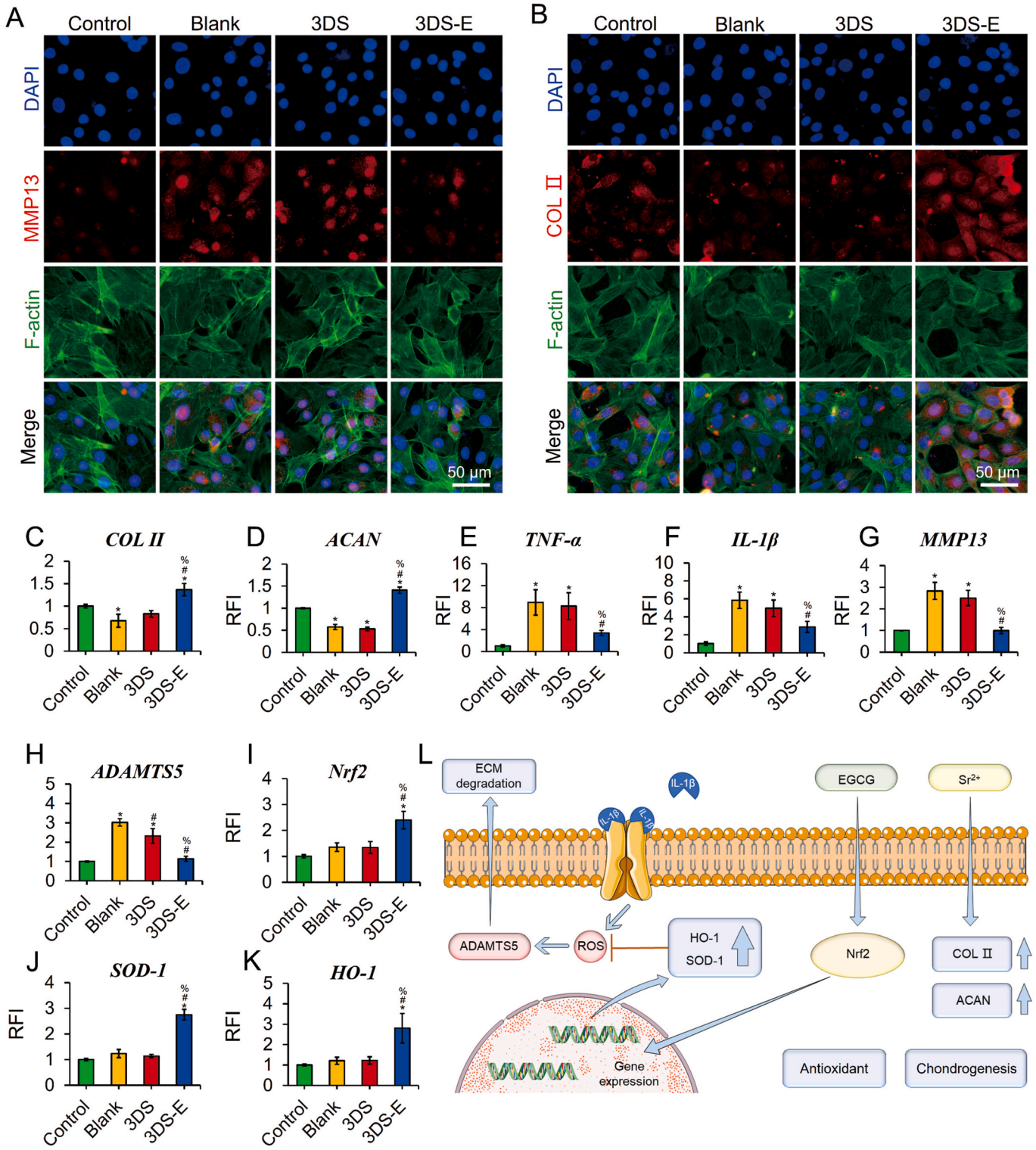

Fig. 6. Chondro-protective properties of scaffolds *in vitro*. Relative expression of MMP13 (A) and COL II (B) in chondrocytes. The mRNA expression level of COL II (C), ACAN (D), TNF-α (E), IL-1β (F), MMP-13 (G), ADAMTS5 (H), Nrf2 (I), SOD-1 (J), and HO-1 (K) in chondrocytes (n = 3). (L) Schematic of the chondro-protective effect of 3DS-E in an inflammatory environment, which inhibited IL-1β-induced ECM degradation through Nrf2/SOD-1, HO-1 pathway. (*, #, % indicate $p < 0.05$ versus control, blank, 3DS.)

cartilage matrix remodeling, strontium also promotes the chondrogenic differentiation of stem cells [37]. Moreover, strontium has been proven to inhibit pro-inflammatory cytokines expression by modulating macrophage phenotype [38,39]. Enhanced cartilage formation in the 3DS-E group may be concurrently associated with strontium release promoting secretion of cartilage matrix. Although this study has demonstrated effective results of 3DS-E in rabbit joint cartilage repair, further research is necessary to assess its regenerative capabilities in larger animals. The mechanical properties of the gas foam scaffold are currently suboptimal, and enhancing these properties through in-situ

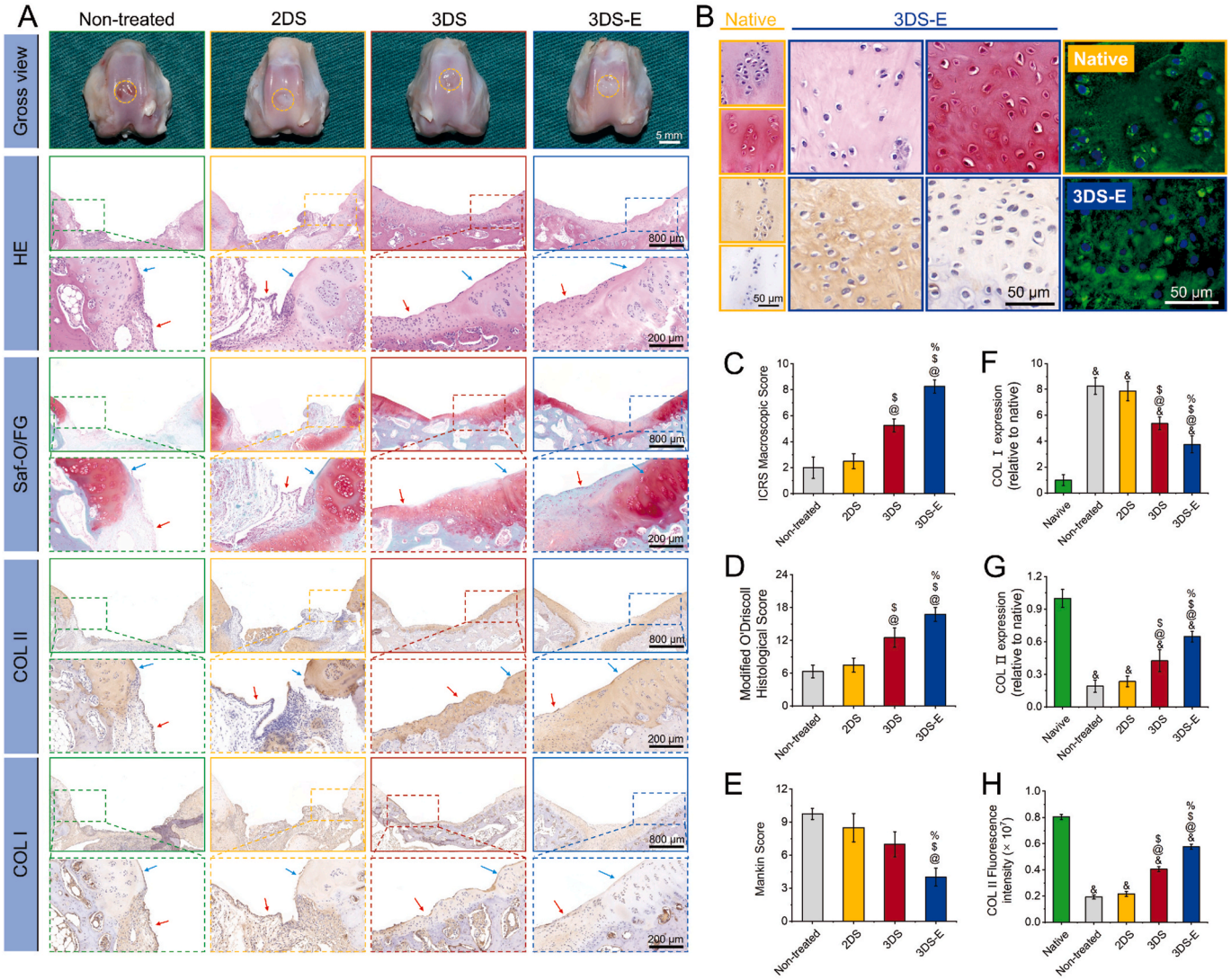

Fig. 7. Cartilage regeneration *in vivo* 12 weeks after surgery. (A) Gross view, H&E, Saf-O/FG, COL II and COL I immunohistochemical staining of cartilage. (B) Magnified staining of native cartilage and regenerative neo-cartilage tissue in 3DS-E at 12 weeks post-surgery. ICRS macroscopic assessment score (C), modified O'Driscoll histological score (D) and Mankin score (E) of regenerative cartilage (n = 4). Relative expression of COL I (F) and COL II (G–H) based on immunohistochemical and immunofluorescent staining (n = 3). (@, &, $, % indicate $p < 0.05$ versus non-treated, native, 2DS, 3DS.)

biomineralization and chemical cross-linking could satisfy the demands for hard tissue regeneration. Moreover, the potential development of the gas foam scaffold into a gradient structure that supports osteochondral regeneration represents a promising direction for future applications.

5. Conclusion

In conclusion, we have proposed a porous MPNs-modified 3D nanofibrous scaffold to alleviate inflammation and promote cartilage matrix remodeling for cartilage regeneration. The modified scaffold featured a low density, appropriate porosity, and an integrated multilayer nanofiber structure. The 3D scaffold maintained stable mechanical properties and low cytotoxicity, which supported enhanced cellular proliferation and infiltration in comparison with 2D scaffolds. In contrast to other groups, 3DS-E can better protect chondrocytes in a simulated inflammatory environment, promote the formation of cartilage-specific ECM, decrease cellular apoptosis, and mitigate the inflammatory microenvironment. Overall, the approach of designing bioactive biomimetic scaffolds based on gas foaming and MPNs modification may hold broad implications for CTE applications.

CRediT authorship contribution statement

Yujie Chen: Writing – original draft, Visualization, Validation, Methodology, Investigation, Data curation, Conceptualization. **Wei Xu:** Methodology, Data curation, Conceptualization. **Zhen Pan:** Methodology, Investigation, Data curation. **Bohui Li:** Data curation, Conceptualization. **Xiumei Mo:** Methodology, Conceptualization. **Yucai Li:** Methodology, Investigation. **Jielin Wang:** Methodology. **Yuan Wang:** Methodology. **Zhenyuan Wei:** Methodology. **Yicheng Chen:** Methodology. **Zhaopu Han:** Methodology. **Chen Lin:** Methodology. **Yu Liu:** Visualization, Methodology, Investigation. **Xiaojian Ye:** Writing – review & editing, Methodology, Investigation, Funding acquisition, Conceptualization. **Jiangming Yu:** Investigation, Funding acquisition, Conceptualization.

Declaration of competing interest

The authors declare that they have no known competing financial interests or personal relationships that could have appeared to influence the work reported in this paper.

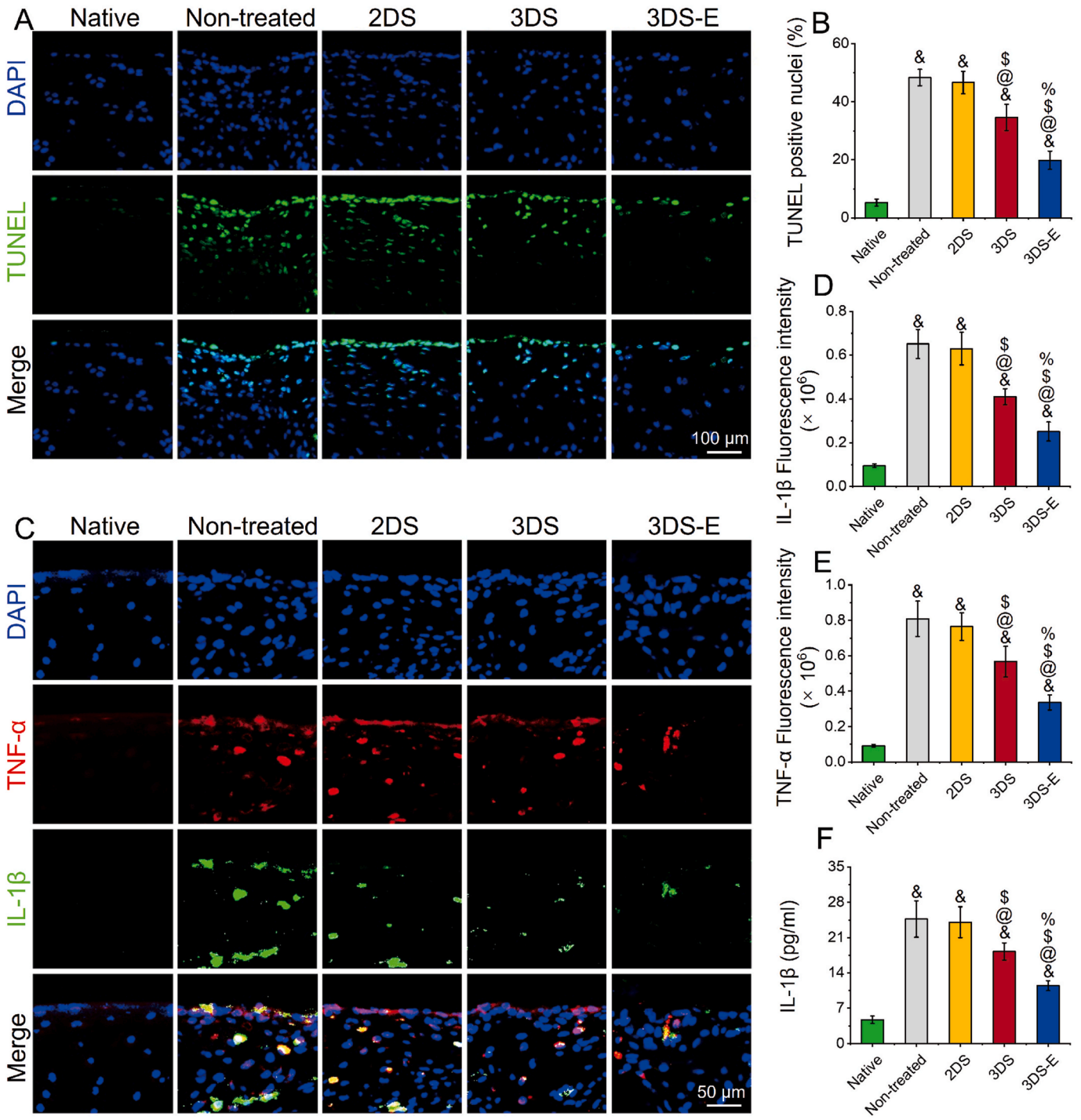

Fig. 8. Chondro-protective abilities of the regenerated cartilage *in vivo*. (A) Chondrocyte apoptosis evaluated by TUNEL staining. (B) TUNEL-positive chondrocytes percentage (n = 3). (C) Immunofluorescent staining of IL-1β and TNF-α in chondrocyte. Fluorescence intensity of IL-1β (D) and TNF-α (E) (n = 3). (F) Concentration of IL-1β determined by ELISA kit (n = 3). (@, &, $, % indicate $p < 0.05$ versus non-treated, native, 2DS, 3DS.)

Data availability

Data will be made available on request.

Acknowledgement

This research was supported by the Science and Technology Commission of Shanghai Municipality (22Y11912000), Medical and Industrial Cross Research Foundation of "Star of Jiaotong University" Program of Shanghai Jiao Tong University, China (Grant No. YG2022ZD030), Laboratory Open Fund of Key Technology and Materials in Minimally Invasive Spine Surgery (2024JZWC-YBA01), Tongren Hospital Introduces.

the Talented Person Scientific Research Start Funds Subsidization Project (TR2023rc08), National Natural Science Foundation of China (82102577), Special Fund for Health Science and Technology of Social Development Shanghai Pudong New Area (PKJ2022-Y20).

Appendix A. Supplementary data

Supplementary data to this article can be found online at https://doi.org/10.1016/j.mtbio.2024.101249.

References

[1] J.J. Vaca-González, J.J.S. Culma, L.M.H. Nova, D.A. Garzón-Alvarado, Anatomy, molecular structures, and hyaluronic acid – gelatin injectable hydrogels as a therapeutic alternative for hyaline cartilage recovery: a review, J. Biomed. Mater. Res. Part B Appl. Biomater. 111 (2023) 1705–1722, https://doi.org/10.1002/jbm.b.35261.

[2] A.A. Elhadad, A. Alcudia, B. Begines, E.M. Pérez-Soriano, Y. Torres, A multidisciplinary perspective on the latest trends in artificial cartilage fabrication to mimic real tissue, Appl. Mater. Today 29 (2022) 101603, https://doi.org/10.1016/j.apmt.2022.101603.

[3] J. Jarecki, M.K. Waśko, W. Widuchowski, A. Tomczyk-Warunek, M. Wójciak, I. Sowa, T. Blicharski, Knee cartilage lesion management—current trends in clinical practice, J. Clin. Med. 12 (2023) 6434, https://doi.org/10.3390/jcm12206434.

[4] A. Anandhapadman, A. Venkateswaran, H. Jayaraman, N. Veerabadran Ghone, Advances in 3D printing of composite scaffolds for the repairment of bone tissue associated defects, Biotechnol. Prog. 38 (2022) 1–19, https://doi.org/10.1002/btpr.3234.

[5] W. Chen, Y. Xu, Y. Liu, Z. Wang, Y. Li, G. Jiang, X. Mo, G. Zhou, Three-dimensional printed electrospun fiber-based scaffold for cartilage regeneration, Mater. Des. 179 (2019) 107886, https://doi.org/10.1016/j.matdes.2019.107886.

[6] W. Chen, Y. Xu, Y. Li, L. Jia, X. Mo, G. Jiang, G. Zhou, 3D printing electrospinning fiber-reinforced decellularized extracellular matrix for cartilage regeneration, Chem. Eng. J. 382 (2020) 122986, https://doi.org/10.1016/j.cej.2019.122986.

[7] Y. Chen, M. Shafiq, M. Liu, Y. Morsi, X. Mo, Advanced fabrication for electrospun three-dimensional nanofiber aerogels and scaffolds, Bioact. Mater. 5 (2020) 963–979, https://doi.org/10.1016/j.bioactmat.2020.06.023.

[8] Y. Chen, X. Dong, M. Shafiq, G. Myles, N. Radacsi, X. Mo, Recent advancements on three-dimensional electrospun nanofiber scaffolds for tissue engineering, Adv. Fiber Mater. 4 (2022) 959–986, https://doi.org/10.1007/s42765-022-00170-7.

[9] J. Jiang, S. Chen, H. Wang, M.A. Carlson, A.F. Gombart, J. Xie, CO_2-expanded nanofiber scaffolds maintain activity of encapsulated bioactive materials and promote cellular infiltration and positive host response, Acta Biomater. 68 (2018) 237–248, https://doi.org/10.1016/j.actbio.2017.12.018.

[10] Y. Chen, W. Xu, M. Shafiq, D. Song, X. Xie, Z. Yuan, M. EL-Newehy, H. EL-Hamshary, Y. Morsi, Y. Liu, X. Mo, Chondroitin sulfate cross-linked three-dimensional tailored electrospun scaffolds for cartilage regeneration, Biomater. Adv. 134 (2022) 112643, https://doi.org/10.1016/j.msec.2022.112643.

[11] Y. Chen, W. Xu, M. Shafiq, J. Tang, J. Hao, X. Xie, Z. Yuan, X. Xiao, Y. Liu, X. Mo, Three-dimensional porous gas-foamed electrospun nanofiber scaffold for cartilage regeneration, J. Colloid Interface Sci. 603 (2021) 94–109, https://doi.org/10.1016/j.jcis.2021.06.067.

[12] H. Slovacek, R. Khanna, P. Poredos, P. Poredos, M. Jezovnik, D. Hoppensteadt, J. Fareed, W. Hopkinson, Interrelationship of MMP-9, proteoglycan-4, and inflammation in osteoarthritis patients undergoing total hip arthroplasty, Clin. Appl. Thromb. 27 (2021) 4–11, https://doi.org/10.1177/1076029621995569.

[13] Z. Yang, H. Li, Z. Yuan, L. Fu, S. Jiang, C. Gao, F. Wang, K. Zha, G. Tian, Z. Sun, B. Huang, F. Wei, F. Cao, X. Sui, J. Peng, S. Lu, W. Guo, S. Liu, Q. Guo, Endogenous cell recruitment strategy for articular cartilage regeneration, Acta Biomater. 114 (2020) 31–52, https://doi.org/10.1016/j.actbio.2020.07.008.

[14] Y. Li, M. Chen, W. Zhou, S. Gao, X. Luo, L. Peng, J. Yan, P. Wang, Q. Li, Y. Zheng, S. Liu, Y. Cheng, Q. Guo, Cell-free 3D wet-electrospun PCL/silk fibroin/Sr^{2+} scaffold promotes successful total meniscus regeneration in a rabbit model, Acta Biomater. 113 (2020) 196–209, https://doi.org/10.1016/j.actbio.2020.06.017.

[15] F. Liu, X. Zhang, X. Yu, Y. Xu, T. Feng, D. Ren, In vitro study in stimulating the secretion of angiogenic growth factors of strontium-doped calcium polyphosphate for bone tissue engineering, J. Mater. Sci. Mater. Med. 22 (2011) 683–692, https://doi.org/10.1007/s10856-011-4247-1.

[16] X. Liao, X. Song, J. Li, L. Li, X. Fan, Q. Qin, C. Zhong, P. Yang, J. Zhan, Y. Cai, An injectable co-assembled hydrogel blocks reactive oxygen species and inflammation cycle resisting myocardial ischemia-reperfusion injury, Acta Biomater. 149 (2022) 82–95, https://doi.org/10.1016/j.actbio.2022.06.039.

[17] S. Xu, L. Chang, X. Zhao, Y. Hu, Y. Lin, Z. Chen, X. Ren, X. Mei, Preparation of epigallocatechin gallate decorated Au-Ag nano-heterostructures as NIR-sensitive nano-enzymes for the treatment of osteoarthritis through mitochondrial repair and cartilage protection, Acta Biomater. 144 (2022) 168–182, https://doi.org/10.1016/j.actbio.2022.03.038.

[18] X. Song, Z. Zheng, S. Ouyang, H. Chen, M. Sun, P. Lin, Y. Chen, Y. You, W. Hao, J. Tao, P. Zhao, Biomimetic rpigallocatechin gallate-cerium assemblies for the treatment of rheumatoid arthritis, ACS Appl. Mater. Interfaces 15 (2023) 33239–33249, https://doi.org/10.1021/acsami.3c02768.

[19] H. Kuang, Y. Wang, Y. Shi, W. Yao, X. He, X. Liu, X. Mo, S. Lu, P. Zhang, Construction and performance evaluation of Hep/silk-PLCL composite nanofiber small-caliber artificial blood vessel graft, Biomaterials 259 (2020) 120288, https://doi.org/10.1016/j.biomaterials.2020.120288.

[20] Y. Chen, W. Xu, M. Shafiq, D. Song, T. Wang, Z. Yuan, X. Xie, X. Yu, Y. Shen, B. Sun, Y. Liu, X. Mo, Injectable nanofiber microspheres modified with metal phenolic networks for effective osteoarthritis treatment, Acta Biomater. 157 (2023) 593–608, https://doi.org/10.1016/j.actbio.2022.11.040.

[21] N. Ninan, A. Forget, V.P. Shastri, N.H. Voelcker, A. Blencowe, Antibacterial and anti-inflammatory pH-responsive tannic acid-carboxylated agarose composite hydrogels for wound healing, ACS Appl. Mater. Interfaces 8 (2016) 28511–28521, https://doi.org/10.1021/acsami.6b10491.

[22] X. Jing, H. Li, H.Y. Mi, Y.J. Liu, Y.M. Tan, Fabrication of fluffy shish-kebab structured nanofibers by electrospinning, CO_2 escaping foaming and controlled crystallization for biomimetic tissue engineering scaffolds, Chem. Eng. J. 372 (2019) 785–795, https://doi.org/10.1016/j.cej.2019.04.194.

[23] Y. Xu, L. Duan, Y. Li, Y. She, J. Zhu, G. Zhou, G. Jiang, Y. Yang, Nanofibrillar decellularized wharton's jelly matrix for segmental tracheal repair, Adv. Funct. Mater. 30 (2020) 1910067, https://doi.org/10.1002/adfm.201910067.

[24] D.W. Tang, S.H. Yu, Y.C. Ho, B.Q. Huang, G.J. Tsai, H.Y. Hsieh, H.W. Sung, F.L. Mi, Characterization of tea catechins-loaded nanoparticles prepared from chitosan and an edible polypeptide, Food Hydrocoll 30 (2013) 33–41, https://doi.org/10.1016/j.foodhyd.2012.04.014.

[25] Y. Li, L.T. Lim, Y. Kakuda, Electrospun zein fibers as carriers to stabilize (-)-epigallocatechin gallate, J. Food Sci. 74 (2009) 233–240, https://doi.org/10.1111/j.1750-3841.2009.01093.x.

[26] S. Selvaraj, N.N. Fathima, Fenugreek incorporated silk fibroin nanofibers - a potential antioxidant scaffold for enhanced wound healing, ACS Appl. Mater. Interfaces 9 (2017) 5916–5926, https://doi.org/10.1021/acsami.6b16306.

[27] X. Xie, Y. Chen, X. Wang, X. Xu, Y. Shen, A. ur R. Khan, A. Aldalbahi, A.E. Fetz, G. L. Bowlin, M. El-Newehy, X. Mo, Electrospinning nanofiber scaffolds for soft and hard tissue regeneration, J. Mater. Sci. Technol. 59 (2020) 243–261, https://doi.org/10.1016/j.jmst.2020.04.037.

[28] Y. Jung, M.S. Park, J.W. Lee, Y.H. Kim, S.H. Kim, S.H. Kim, Cartilage regeneration with highly-elastic three-dimensional scaffolds prepared from biodegradable poly (l-lactide-co-ε-caprolactone), Biomaterials 29 (2008) 4630–4636, https://doi.org/10.1016/j.biomaterials.2008.08.031.

[29] S. Çalamak, C. Erdoğdu, M. Özalp, K. Ulubayram, Silk fibroin based antibacterial bionanotextiles as wound dressing materials, Mater. Sci. Eng. C 43 (2014) 11–20, https://doi.org/10.1016/j.msec.2014.07.001.

[30] Y. Li, M. Chen, J. Yan, W. Zhou, S. Gao, S. Liu, Q. Li, Y. Zheng, Y. Cheng, Q. Guo, Tannic acid/Sr^{2+}-coated silk/graphene oxide-based meniscus scaffold with anti-inflammatory and anti-ROS functions for cartilage protection and delaying osteoarthritis, Acta Biomater. 126 (2021) 119–131, https://doi.org/10.1016/j.actbio.2021.02.046.

[31] H. Liang, Y. Pei, J. Li, W. Xiong, Y. He, S. Liu, Y. Li, B. Li, pH-Degradable antioxidant nanoparticles based on hydrogen-bonded tannic acid assembly, RSC Adv. 6 (2016) 31374–31385, https://doi.org/10.1039/c6ra02527g.

[32] I.P.S. Fernando, M. Kim, K. Son, Y. Jeong, F.E.T. Al, Antioxidant activity of marine algal polyphenoliccompounds: a mechanistic approach, J. Med. Food 19 (2016) 1–14, https://doi.org/10.1089/jmf.2016.3706.

[33] M. Li, H. Yin, Z. Yan, H. Li, J. Wu, Y. Wang, F. Wei, G. Tian, C. Ning, H. Li, C. Gao, L. Fu, S. Jiang, M. Chen, X. Sui, S. Liu, Z. Chen, Q. Guo, The immune microenvironment in cartilage injury and repair, Acta Biomater. 140 (2022) 23–42, https://doi.org/10.1016/j.actbio.2021.12.006.

[34] Z. Cao, H. Wang, J. Chen, Y. Zhang, Q. Mo, Silk-based hydrogel incorporated with metal-organic framework nanozymes for enhanced osteochondral regeneration, Bioact. Mater. 20 (2023) 221–242, https://doi.org/10.1016/j.bioactmat.2022.05.025.

[35] R. Lin, C. Deng, X. Li, Y. Liu, M. Zhang, C. Qin, Q. Yao, L. Wang, C. Wu, Copper-incorporated bioactive glass-ceramics inducing anti-inflammatory phenotype and regeneration of cartilage/bone interface, Theranostics 9 (2019) 6300–6313, https://doi.org/10.7150/thno.36120.

[36] Y. Henrotin, A. Labasse, S.X. Zheng, P. Galais, Y. Tsouderos, J.M. Crielaard, J. Y. Reginster, Strontium ranelate increases cartilage matrix formation, J. Bone Miner. Res. 16 (2001) 299–308, https://doi.org/10.1359/jbmr.2001.16.2.299.

[37] N. Xu, D. Lu, L. Qiang, Y. Liu, D. Yin, Z. Wang, Y. Luo, C. Yang, Z. Ma, H. Ma, J. Wang, 3D-Printed composite bioceramic scaffolds for bone and cartilage integrated regeneration, ACS Omega 8 (2023) 37918–37926, https://doi.org/10.1021/acsomega.3c03284.

[38] F. Zhao, B. Lei, X. Li, Y. Mo, R. Wang, D. Chen, X. Chen, Promoting in vivo early angiogenesis with sub-micrometer strontium-contained bioactive microspheres through modulating macrophage phenotypes, Biomaterials 178 (2018) 36–47, https://doi.org/10.1016/j.biomaterials.2018.06.004.

[39] M. Fenbo, X. Xingyu, T. Bin, Strontium chondroitin sulfate/silk fibroin blend membrane containing microporous structure modulates macrophage responses for guided bone regeneration, Carbohydr. Polym. 213 (2019) 266–275, https://doi.org/10.1016/j.carbpol.2019.02.068.